High-Efficiency Automated Nanomanipulation with Parallel Imaging/Manipulation Force Microscopy

Hui Xie, *Member, IEEE,* and Stéphane Régnier

Abstract—The atomic force microscope (AFM) has been widely used to manipulate nanoparticles, nanowires and nanotubes for applications, such as, nano-structure building, nano-characterization and bio-manipulation. However, conventional AFM-based nanomanipulation is inefficient because of the serial scan-manipulation-scan process involved. In this paper, high-efficiency automated nanomanipulation with a parallel imaging/manipulation force microscope (PIMM) is presented. With the PIMM, image scan and nanomanipulation can be performed in parallel through the collaboration between two cantilevers: one cantilever acts as an imaging sensor and the other is used as a manipulating tool. Two automated manipulation schemes were introduced for normal- and high-speed image scanning, respectively. An automated parallel manipulation task is managed by system control software with multi-thread through a procedure of dynamic image processing, task planning, two-tip collaboration, and a controlled pushing manipulation with amplitude feedback from the cantilevers. The efficiency of automated parallel nanomanipulation with normal-speed image scanning was validated by building nanoparticle patterns.

Index Terms—Atomic force microscope, parallel nano manipulation, automated, high efficiency, nano particle push.

I. INTRODUCTION

THE invention of the atomic force microscope (AFM) has brought nanotechnology with a significant boost by providing it with a powerful tool for understanding physical and chemical phenomena at the nanoscale to atomic scale, as well as for performing engineering operations on nano-objects, molecules and atoms. After the first manipulation of atoms was accomplished using STM about two decades ago [1], various nanomanipulation and nanoassembly schemes and systems have been introduced. Conventional AFM has been by far the most widely applied for the manipulation or characterization of nanomaterials [2]–[6] and biology samples [7], [8]. Moreover, AFM has also been used to explore nanoscale characterization, e.g., nanotribology [9], [10] and nanowire shear stress measurement [11]. However, AFM-based manipulation has an inherent limitation, namely, the imaging and manipulation processes are performed in series. In other words, AFM-based nanomanipulation generally involves an insufficient scan-manipulation-scan process, which makes mass production impossible. The reasons for this can generally be attributed to insufficient AFM-based nanomanipulation: first, unlike manipulation carried out in a electron microscope [12], the AFM has no real-time visual feedback, and, second, low-speed image scanning using conventional AFMs also involves a time-consuming nanomanipulation process.

To facilitate nanomanipulation with interactive feedback, haptic devices and virtual reality interfaces were introduced into AFM-based nanomanipulation systems [13], [14], thereby enabling an operator to directly interact with the real nano world to control the manipulation process. Nevertheless, for haptic interface initialization and for validation of the manipulation, the pre-manipulation and post-manipulation images are still required. On the other hand, in order to enhance image-scanning efficiency, several researches have provided impressive demonstrations of high-speed AFMs [15]–[17]. Many applications in materials science, life science and process control have benefited from the AFM with higher speed scanning. However, high-speed AFM applications are limited, since only a small number of dedicated research labs have high-speed AFMs that are highly specialized. Moreover, the excellent potential for imaging will be greatly reduced if the high-speed AFM is used for nanomanipulation when a serial scan-manipulation-scan process is still involved.

The central problem in speeding up AFM-based nanomanipulation revolves around how to develop sufficient harmony between the image scan and manipulation processes of AFM-based nanomanipulation. As manipulation performed under optical microscopes or electron microscopes, the standard parallel imaging/manipulation method still offers promise for improving the efficiency of AFM-based nanomanipulation if the image scan and manipulation can be carried out in parallel.

In this paper, a modified two-tip AFM, called parallel imaging/manipulation force microscope (PIMM) is introduced to improve the efficiency of AFM-based nanomanipulation. A key component of the PIMM is that two individually actuated cantilevers are used independently for imaging and nanomanipulation, thereby enabling parallel nanomanipulation and making high-efficiency nanofabrication feasible. This research, based on our previous work on the development of the PIMM [18], focuses on: (i) Automating parallel imaging/nanomanipulation by introducing effective manipulation strategies and control schemes, including image processing and feature recognition, tasking planning for both the normal- and high-speed image scan, and nanorobotic control for two tips coordination with coordinate transformations and detailed

control flows; (ii) Introducing a dynamic pushing method for automated particle loss detection using amplitude feedback rather than the weak lateral force signal and the unstable normal force signal of the optical lever; (iii) Comparing efficiencies of automated serial and parallel nanomanipulation with experimental results; (iv) Performing a more complicated parallel nanomanipulation task with presented manipulation strategies and control schemes to validate the proposed parallel nanomanipulation method.

This paper is organized as follows: Section II briefly introduces the prototype and experimental setup of the PIMM. Two parallel manipulation schemes respectively with normal- and high-speed image scanning are presented in section III. Control flow and methods are introduced in section IV. In section V, we use one-tip and two-tip configurations of the PIMM to respectively complete serial and parallel nanomanipulation of nanoparticles to form nano-patterns with normal-speed image scanning. Section VII concludes the paper.

II. SYSTEM SET-UP OF THE PIMM

A. System Architecture

Figure 1 shows a schematic diagram of the developed PIMM. Cantilever I (tip I) and cantilever II (tip II), facing each other, are individually actuated by an open-loop X-Y-Z piezoscanner (PI P-153.10H) and an X-Y-Z closed-loop nanostage (MCL Nano-Bio2M on the X-Y axes, PI P-732.ZC on the Z-axis), respectively. An X-Y-Z motorized stage and an X-Y-Z manual stage are used for coarse positioning of tip I and tip II, respectively. The sample platform is immovable during manipulation that is fixed on the system base.

A data acquisition (DAQ) (NI 6289) card is used for high-speed capturing of photodiode voltage output from a lock-in to estimate deflections on both cantilevers induced by force load or resonant oscillation. The DAQ card is also used to actuate the piezoscanner by providing voltage signals to three independent amplifiers for each axis. A multi-thread planning and control system is developed to independently manage the AFM image scan and its dynamic display and processing, as well as two-tip coordination during parallel imaging/manipulation. Scanning data, a topographic image including nano-objects to be manipulated and the end of tip II, are shared by each of the threads for manipulation planning and system control.

B. Two-Tip Interactions

A key component of the PIMM is that the cantilever used has a protruding tip, which makes interactions between both cantilevers feasible. As shown in Fig. 2(a), the protruding tip enables image scan on the end of tip II using tip I. An AFM image of the end of tip II is shown in Fig. 2(b), in which the left inset shows a simulated scanning height when tip I is scanned tip II along the line a–a. By this means, the relative positions between the nano-objects and the end of tip II that is indispensable for AFM-based nanomanipulation can be obtained from the image scan. The tilted angle of the tip is approximately $63°$ on the side view. In the PIMM, the final tilted angle of each tip is about $68°$ to the substrate with a
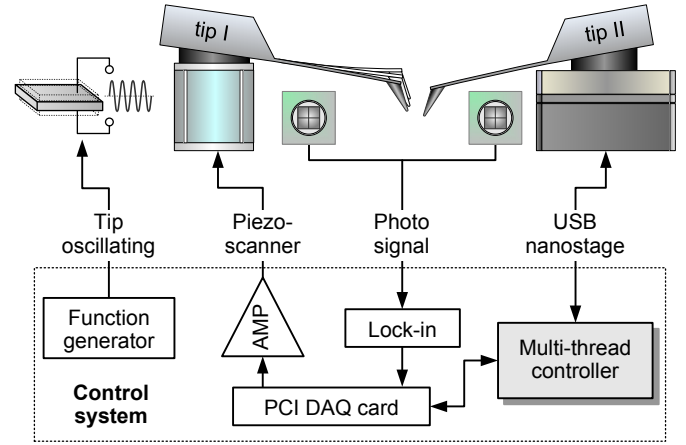

Fig. 1. System setup of the PIMM and a schematic diagram of the architecture of the control system.
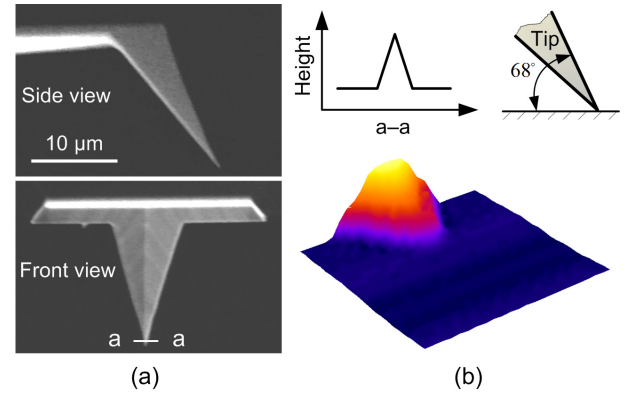

Fig. 2. Two tip interaction during the image scan. (a) An SEM image of tip's side and front view, in which a–a is a trace scanned at the end of tip II by tip I. (b) A topographic AFM image of the tip end. The left inset shows a simulated height of tip end on the scan line a–a, and the right inset shows the tip has a tilted angle of $68°$ with a mounting angle of $5°$.

mounting angle of $5°$, as seen in the right inset of Fig. 2(b). Thus, the scanning height of tip II can be estimated as:

$$H_t = L_t \tan 68° \approx 2.48 L_t \qquad (1)$$

where H_t and L_t are the scan height and the scan length on tip II, respectively. Excellent image quality can be achieved even though L_t is more than 300 nm, which is sufficient for tip positioning during the manipulation.

C. Coordinate Frames

Figure 3(a) shows coordinate frames of the PIMM that are summarized in Table II, including image scan frame s, manipulation frame m and image frame i. A point $P = (X, Y, Z)$ in the system coordinate X-Y-Z is mapped to a point $p = (u, v)$ in the image plane X_i-O_i-Y_i via a scaled orthographic projection:

$$\begin{bmatrix} p_x & 0 \\ 0 & p_y \end{bmatrix} \begin{bmatrix} u \\ v \end{bmatrix} = \begin{bmatrix} X \\ Y \end{bmatrix} \qquad (2)$$

where p_x and p_y are scale factors, which are physical dimensions of pixels in the horizontal and vertical directions,
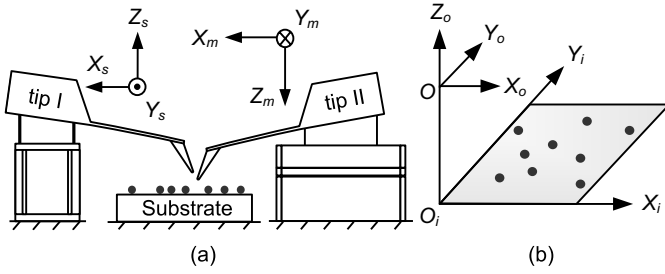
Fig. 3. (a) Coordinate frames of the system. (b) The coordinate frame of the image plane.

TABLE I
SPECIFICATIONS OF COORDINATE FRAMES

Symbol	Coordinate frame definition
s	Imaging cantilever (tip I) coordinate frame X_s-Y_s-Z_s attached to the piezoscanner
m	Manipulating cantilever (tip II) coordinate frame X_m-Y_m-Z_m attached to the nanostage
o	Coordinate frame X_o-O_o-Y_o of the system
i	Coordinate frame X_i-O_i-Y_i of the scanned image plane

respectively. Each scale factor is equal to the step length (s_x, s_y) of the image scan on the corresponding axis. The step lengths are determined by the resolution (r_x, r_y) and the length (l_x, l_y) of the scanned image:

$$
\begin{bmatrix} s_x \\ s_y \end{bmatrix} = \begin{bmatrix} 1/r_x & 0 \\ 0 & 1/r_y \end{bmatrix} \begin{bmatrix} l_x \\ l_y \end{bmatrix}. \tag{3}
$$

Therefore, the point $P = (X, Y, Z)$ in the system coordinate X-Y-Z can be determined by the point $p = (u, v)$ in the image plane X_i-O_i-Y_i via:

$$
\begin{bmatrix} X \\ Y \end{bmatrix} = \begin{bmatrix} 1/r_x & 0 \\ 0 & 1/r_y \end{bmatrix} \begin{bmatrix} l_x & 0 \\ 0 & l_y \end{bmatrix} \begin{bmatrix} u \\ v \end{bmatrix}. \tag{4}
$$

III. STRATEGIES FOR AUTOMATED PARALLEL MANIPULATION

As mentioned above, image scanning with the cantilever's protruding tip makes it possible to locate the nano-objects as well as the tip end of the manipulating cantilever, providing positioning information for the further task planning. A manipulation protocol and two schemes are introduced respectively for parallel nanoparticle push with normal- and high-speed image scanning. Task planning based on the shortest path solution is proposed for linear trajectory planning on nano-pattern formations.

A. Parallel Imaging/Manipulation Protocol

A manipulation protocol is used to perform the image scan and the nanomanipulation in parallel. This protocol mainly includes the following steps,

1) System Initialization: In this step, both tips are aligned near the starting point of the selected scan area under the optical microscope. Each axis of the motion module is set on a proper position in the frames defined in Fig. 3. The initialization should provide enough motion travel for both the image scan and the manipulation.

2) Local Scanning on Tip II: Before the task, local image scan with tapping mode of tip I is used to locate the end of tip II. As seen in (1), the scanning length on tip II is determined by its scanning height, which should have a maximum image height roughly equals to the nano-objects to be manipulated.

3) Parallel Nanomanipulation: Once the local scanning of tip II is completed, tip I is activated to fully scan the region of interest, obtaining a topographic image that contains nano-objects to be manipulated and the end of tip II. Simultaneously, tip II is also managed by the manipulation control thread. After image processing and task planning, the nano-objects are manipulated with a controlled pushing operation. This step will be discussed in detail in the following sections.

B. Image Processing

Image processing is for task planning and the coarse positioning of each nanoparticle. Two steps are involved in the image processing: recognize nanoparticle distribution and calculate their central positions. Fig. 4(a) shows an AFM image, which contains the end of tip II and ten nanoparticles with a diameter of about 80 nm.

1) Recognition Nanoparticles and the End of Tip II: A feature in the scanned image may be a nanoparticle or the end of tip II. In order to recognize and classify these features, the template-matching method via correction coefficient $\gamma(x, y)$ is used [19]:

$$
\gamma(x, y) = \frac{\sum_s \sum_t \left[(f - \bar{f}) \right] \left[(w(x + s, y + t) - \bar{w}) \right]}{\sqrt{\sum_s \sum_t \left[(f - \bar{f}) \right]^2 \sum_s \sum_t \left[(w(x + s, y + t) - \bar{w}) \right]^2}} \tag{5}
$$

where x and y are the width and height of the scanner image, $\bar{w}$ is the average gray value of the template window w, and $\bar{f}$ is the average gray value of the image f in the region coincident with the current location w. Using pre-defined templates, the nanoparticles and the end of tip II can be easily identified.

2) Positioning Nanoparticles and the End of Tip II: The AFM image is first convolved with a low-pass Gaussian filter for noise suppression, and then segmented to a binary image using the optimal global and adaptive thresholding method [19]. For further processing, the binary image is eroded to remove overly small or large areas that represent spurious or connected features with several nanoparticles stuck together.

Then the region-growing method [19] is used to label each feature and calculate its central position. After region-growing, each of the regions has certain gray values for feature identification. For each labeled feature, its center position $(\bar{x}_k, \bar{y}_k)$ can be calculated as:

$$
\bar{x}_k = \frac{\sum_{j=1}^{m_k} x_j}{m_k} , \qquad \bar{y}_k = \frac{\sum_{j=1}^{m_k} y_j}{m_k} \tag{6}
$$

where x_j is the x-coordinate and y_j is the y-coordinate of pixel j of the kth region that contains m_k pixels. Fig. 4(b) shows an image after region growing. Eleven features, including ten nanoparticles and the tip II end, are labeled from 1 to 10 by gray value 74 to 254 with an interval of 20 for the
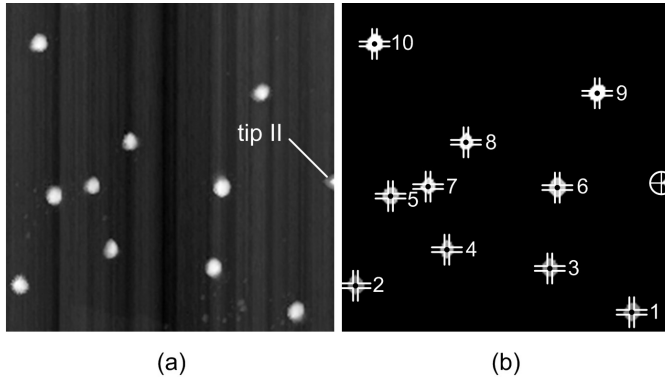
Fig. 4. An example of image processing. (a) An original gray-lever image with a scan area 5 μm × 5μm. (b) A binary image by global and adaptive thresholding; features are labeled and their centers are located.

Fig. 5. Parallel imaging/nanomanipulation scheme with normal-speed image scan.

nanoparticles and gray value 255 for the end of tip II. If the number of nanoparticles is more than 255, feature labeling is performed within each sub-region of the image grid.

Once the features are characterized and their center positions are calculated, nanoparticles $p_k(k = 1, 2, \ldots, n)$, assuming k is a unique ID for each nanoparticle and its position in the image plane is denoted as $p_k = (\bar{x}_k, \bar{y}_k)$ for task planning of nano-pattern formation.

C. Manipulation Scheme with Normal-Speed Image Scan

The AFM tapping mode is required for nanoparticle scanning in ambient conditions, to avoid the tip from moving or removing the nanoparticle as it scans them. Several minutes should then be taken for a full image scan using normal-speed scanning. In this case, the image display is updated pixel-by-pixel with the data sampling frequency, tracking the scan motion of tip I.

1) Manipulation Scheme: Figure 5 is a diagram of parallel imaging/manipulation with normal-speed image scanning. As for the parallel imaging/manipulation protocol mentioned above, once tip II locating is ready, two parallel threads are started to perform a parallel imaging/manipulation task. One is used to control tip I to complete a full scan of the pertinent area selected under the optical microscope, resulting in a topographic image containing nanoparticles to be manipulated as well as the end of tip II (as a simulated image on position P_{II}^0). The second thread is assigned to dominate the performance of tip II, which is in idle process until a particle emerges on the dynamic image display. As the predetermined target positions t_1 and t_2 as well as at least one nanoparticle are entirely scanned as tip I reaches position P_{I}^1, the first manipulation is started after the approximate position of particle I is estimated by processing the dynamic image.

In order to accurately position nanoparticle p_1, tip II locally scans the nanoparticle horizontally and vertically along a line marked to locate the precise center of the nanoparticle and estimate a pushing point. As tip II reaches $P_{\mathrm{II}}^{s_1}$, that is on the line connecting centers of p_1 and t_1, the manipulation is started until tip II reaches $P_{\mathrm{II}}^{g_1}$ where particle p_1 has been pushed to the target position. After the first manipulation, tip II is started again to manipulate particle p_2 to its target position
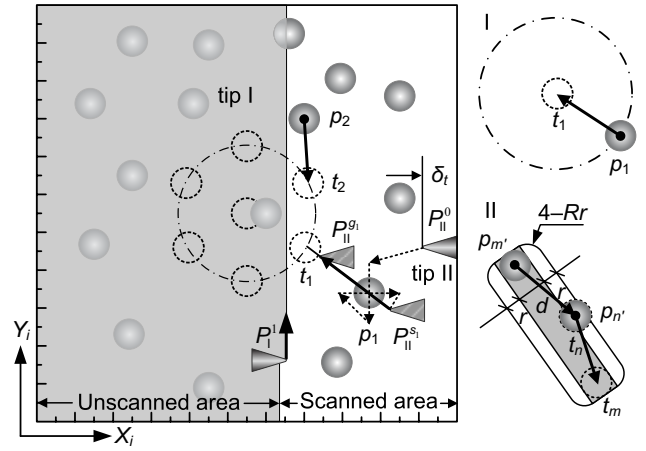
t_2. When the second manipulation is completed, tip II is set to idle process again until new target positions and nanoparticles for manipulation emerge.

2) Task Planning: With normal-speed image scanning, global task planning is unavailable during manipulation due to the very low imaging rate. However, parallel imaging/nanomanipulation can certainly be performed if a manipulation objective is defined before the operation. As shown in Fig. 5, prior to the nanomanipulation, a regular hexagon pattern is predetermined within the image plane X_i–Y_i. As corners of the regular hexagon emerge on the dynamic image display and nanoparticles are present, the shortest path solution is used to plan the linear trajectory of the nanoparticle's motion.

As seen in inset I, the nanoparticle p_1, which has the shortest distance to t_1, is chosen as the first to be manipulated. The target position sequences are determined along the y-axis of the image coordinate frame when more than one target position emerges on the same effective image area, e.g. t_1 and t_2. During the whole process of parallel nanomanipulation, previously manipulated nanoparticles, which are in their target positions, are at times probably viewed as obstacles. As shown in inset II of Fig. 5, the manipulated nanoparticle $p_{n\prime}$, on its target position t_n, is within the obstacle zone of the nanoparticle $p_{m\prime}$ and its target position t_m. In this case, if no other nanoparticles exist within the currently scanned area, these two nanoparticles should exchange their target positions by removing $p_{n\prime}$ to t_m and $p_{m\prime}$ to t_n. The width of the obstacle zone is set at twice the diameter of the nanoparticle because of the possibility of the nanoparticle rotating around the AFM tip during the pushing operation.

D. Manipulation Scheme with High-Speed Image Scan

Unlike normal-speed image scanning, high-speed image scanning is expected to provide an image rate from several frames per second to video rate. In this case, image display can be updated rapidly. For task planning, image processing is performed for every frame of the image scan from the beginning.
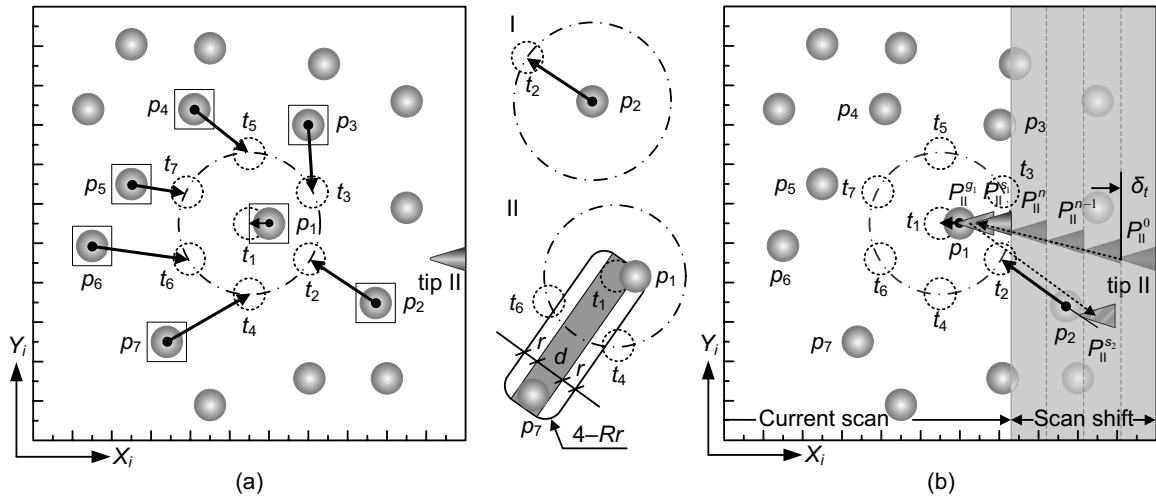
Fig. 6.   Strategies for parallel nanomanipulation with high-speed image scan. (a) Simulated trajectory planning using the first frame of high-speed image scan. (b) Parallel imaging/nanomanipulation scheme with high-speed image scan.

1) Task Planning: With high-speed image scanning, global task planning is available that is performed and can be the first of scan frame. Fig. 6(a) shows the first frame of simulated topographic image that contains nanoparticles and the end of tip II. After image processing of this frame, trajectory planning is started to generate a manipulation sequence for each target position and the corresponding nanoparticle to be manipulated. The trajectory-planning algorithm is summarized as follow:

1) Share one frame of image from the imaging thread.
2) Detect the central position of each nanoparticle in the image space using the method mentioned above.
3) Determine an equal number of particles with the target positions.
4) Generate a manipulation sequence for the target positions.
5) **for** $k = 1$ to N (number of targets)
   a) Generate all possible linear trajectories between each particle and the target position $t_k(x_i, y_i)$ in the image space.
   b) Select the particle with a central position on $(x_i, y_i)(n = 1, 2, \ldots, N)$ that has the shortest path to the target position t_k.
   end for
6) Transform the position sequences $t_k(x_i, y_i)/p_n(x_i, y_i)$ from the image coordinate frame X_i-O_i-Y_i into manipulation coordinate frame X_m-Y_m-Z_m for actual motion planning of the nanomanipulation.

Since linear trajectory is more convenient than nonlinear for pushing nanomanipulation with a single nanotip, an efficient strategy was proposed for 2-D micro manipulation with a single probe [20]. In order to avoid losing the least problematic particles those have the shortest paths to the target positions, a strategy is introduced to combine distance planning with the method mentioned above. With this strategy, the shortest path method is used first to generate an equal number of particles with the reference target positions for trajectory planning only if there are more particles than target positions, as shown in inset I. Then by counting the number of the blockages of

each target position to every previously selected particle, a manipulation sequence of the target positions is determined. Inset II shows an example for target position t_1, with three blockages counted with a possible trajectory to particle p_7. Finally, the shortest path method is used to find a particle for each target position with the generated sequence.

Once the trajectory planning is completed, for each of the target positions in sequence, tip II is used to push the nearest nanoparticle along the generated trajectories. Fig. 6(a) shows a predetermined nano-pattern formed by a regular hexagon with a central particle. Six nanoparticles labeled p_1 to p_6 are chosen to build this nano-pattern.

2) Manipulation Scheme: Figure 6(b) shows a diagram of the parallel manipulation with high-speed image scan. Tip I is used for high-speed image scanning of the nanoparticles and the end of tip II, producing a high-speed topographic image display, which consists of tip II and nanoparticles to be manipulated. After task planning, tip II is started to approach nanoparticle p_1 for the first manipulation after the first frame of the dynamic image display. Simultaneously, the scan area is dynamically shifted by tracking the motion of tip II to keep a fixed scan length δ_t on tip II for to avoid blocking the image scan due to excessive scan height on the end of tip II. The scan area is shifted from P_{II}^0 to P_{II}^n until tip II reaches $P_{II}^{s_1}$, at which point the manipulation is started to push nanoparticle p_1 to its target t_1 while tip II travels to $P_{II}^{g_1}$. After the first manipulation, tip II is moved on to the next nanoparticle.

E. Comparing Manipulation with Different Scan Rates

Obvious differences between the parallel nanomanipulation with normal- and high-speed scanning are summarized as:

1) Different Task Planning Methods: Task planning with normal-speed scanning is limited in local areas due to its low imaging rate. In contrast, with high-speed image scanning, the global task planning is available and, if necessary, dynamic task planning is feasible with high-speed visual feedback that provides more accurate and efficient trajectory planning for pattern formation.
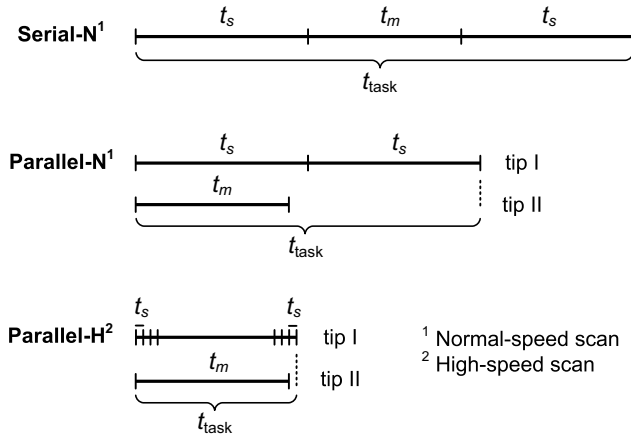
Fig. 7.   The timing model of serial conventional AFM-based nanomanipulation, and parallel nanomanipulation with normal- and high-speed image scanning.

2) Incomparable Manipulation Robustness: High-speed imaging rate make the parallel nanomanipulation more controllable due to its visual feedback, which can be used to track the nanoparticle's motion, monitor the tip-nanoparticle interactions, and compensate for system error induced by thermal drift. Combining visual feedback with force and amplitude feedback from the oscillating tip, the parallel manipulation control with high-speed image scan is undoubtedly more stable and robust.

3) Dissimilar Task Time: The comparison between the manipulation with normal- and high-speed image scanning centers around the manipulation efficiency. As shown in Fig. 7, task time t^p_{task} of the parallel imaging/manipulation can be given as:

$$t^p_{\text{task}} = \max(t_s, t_m) + t_s \tag{7}$$

where t_s is the scanning time of one image frame and t_m is the total manipulation time estimated from the sum of manipulation time of each single nano-object. For normal-speed AFM, the task time is often equal to $2t_s$ except for a complicated manipulation task that cannot be completed within one frame period, and so has task time of $t_m + t_s$. The task time with high-speed AFM is approximately equal to the total manipulation time t_m due to the very high frame rate of the image scan. The manipulation process in this scheme is monitored by the high-speed visual feedback like the manipulation performed in the SEM. The parallel nanomanipulation with high-speed image scan is undoubtedly more efficient than normal-speed image scanning.

In contrast, the task time t^s_{task} in the serial imaging/manipulation operation:

$$t^s_{\text{task}} = t_m + 2t_s. \tag{8}$$

From (7) and (8), it is found that with the normal-speed image scan the parallel nanomanipulation can save a lot of time, e.g., when $t_m = t_s$, task time of the serial nanomanipulation will increase by 50% compared with the parallel nanomanipulation.

IV. Automated Control of the Parallel Nanomanipulation

A. Nanorobotic Control on Both Tips

Once the manipulation thread is started, the motion control of tip II is based on the position information from the image scan, irrespective of normal- or high-speed image scanning. There is the difference, however, that high-speed image scanning provides dynamic image feedback to track the motion of tip II and the nanoparticle being manipulated, compared with normal-speed image scanning in which the positions of tip II and the nanoparticles to be manipulated are just generated once before the manipulation. As discussed in section III-B, feature recognition from image processing is performed to identify the nano-particle position T_i, in which case control is in the form of manipulation under the optical microscope using the "look-then-move" strategy. In order to determine the kinematic parameters of tip II from image recognition, coordinate transformations are performed between coordinate frames of the image plane and the tips.

Denote $^oP \in \Re^2$ the coordinate of point P with respect to coordinate frame o; Denote $^m_oR \in \Re^{2\times2}$ the rotation matrix that represents the orientation of frame o with respect to frame m; Denote $^m_oT \in \Re^2$ the origin location of frame o with respect to frame m

$$^mP = {}^m_oR\,{}^oP + {}^m_oT,$$

$$^sP = {}^s_oR\,{}^oP + {}^s_oT. \tag{9}$$

Re-writing (4)

$$^i_sP = {}^oP \tag{10}$$

where

$$s = \begin{bmatrix} 1/r_x & 0 \\ 0 & 1/r_y \end{bmatrix} \begin{bmatrix} l_x & 0 \\ 0 & l_y \end{bmatrix}.$$

From (9) and (10)

$$^mP = {}^m_oR\,{}^i_sP + {}^m_oT,$$

$$^sP = {}^s_oR\,{}^i_sP + {}^s_oT. \tag{11}$$

According to the coordinate frames defined in Fig. 3

$$^m_oR = \begin{bmatrix} -1 & 0 \\ 0 & 1 \end{bmatrix}, \quad {}^s_oR = \begin{bmatrix} -1 & 0 \\ 0 & -1 \end{bmatrix}. \tag{12}$$

With a known s, the transformations between frame i, frame m and frame s are uniquely determined by ^s_oT and ^m_oT. ^m_oT is solved from ^mP and ^iP, as tip II position is identified after image processing. Similarly, ^s_oT is solved from ^sP and ^iP with known dimensions of the image scan.

B. Control Flow

The control system is developed upon the platform C++, in which two subsidiary threads are respectively established for image scanning and manipulation. The main thread of the task here is used to store the image data and provide the user with an interface with dynamic image display and other real-time data, e.g., force responses from both the cantilevers and position feedback from each of the motion modules.
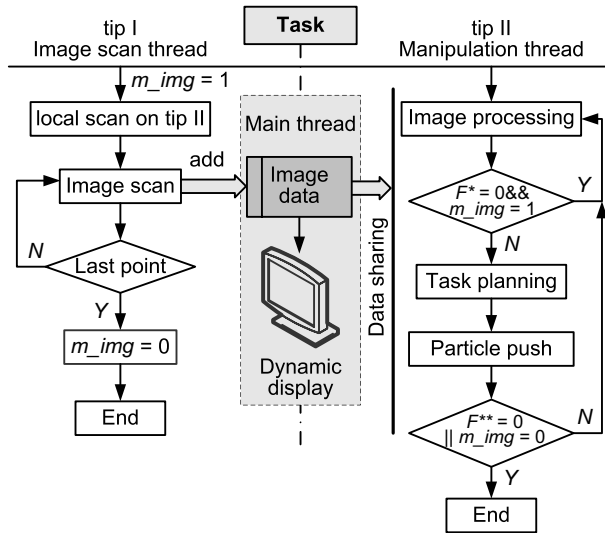
Fig. 8. Control flow of automated parallel nanomanipulation with normal-speed image scan. $F^* = 0$ presents a logic: no new target(s) and new nanoparticle(s) emerge; $F^{**} = 0$ presents a logic: no target or no nanoparticle remain. m_img is a global variable used as a switch for image scan.
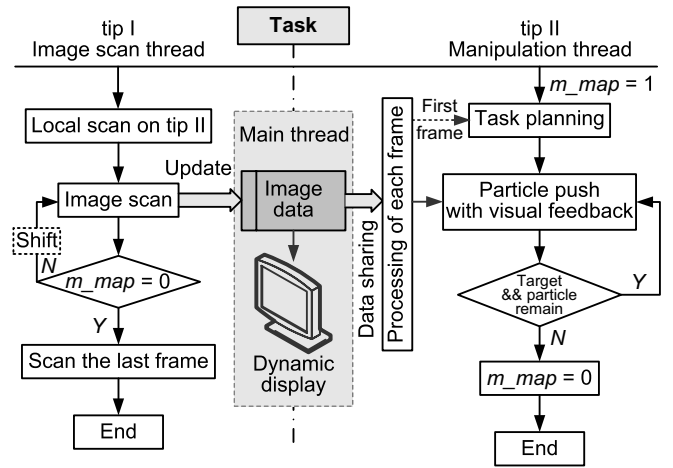
Fig. 9. Control flow of automated parallel nanomanipulation with high-speed image scan. m_map is a global variable used as a switch for parallel nanomanipulation.

Figure 8 shows the control flow of the parallel nanomanipulation with the normal-speed image scanning. In this flow, before the next manipulation, task planning on a newly updated scanned area is performed when new target(s) and new nanoparticle(s) emerge. The image scan thread is ended with the last scan point; meanwhile, m_img is set to zero. The manipulation thread is ended if all the target positions are filled or there are no nanoparticle(s) for the remaining target(s).

Figure 9 shows the control flow with high-speed image scanning, in which image processing is performed for each frame of the scan and the pushing operation are control with visual feedback. The manipulation task is ended if there are no targets or any nanoparticles emerge. m_map here is used as a global switch to end the image scan thread, as it is set to zero when the manipulation is ended. The last frame is scanned as a post-manipulation image. Notice that the next frame of the image scan shifts backwards a distance of δ_{t-1} from the last start point, where δ_{t-1} is tip II's displacement on the x-axis of frame s during last frame period t_s.

C. Force Sensing during the Nanoparticle Push

In experiments, for a cantilever with a beam length L, beam width w, beam thickness t and tip height l, its normal stiffness k_n and lateral stiffness k_l are calculated by:

$$k_n = \frac{Ewt^3}{6L^2} \quad \text{(N/rad)} \tag{13}$$

$$k_l = \frac{Gwt^3}{3L(l + t/2)} \quad \text{(N/rad)} \tag{14}$$

where E and G are, respectively, Young's and shear modulus of the cantilever. Assuming the optical lever has the same angular sensitivities on lateral and normal directions, the ratio of the cantilever's normal and lateral force sensitivities S_{ratio}

can be obtained from (13) and (14):

$$S_{\text{ratio}} = \frac{k_l}{k_n} = \frac{2LG}{E(l + t/2)}. \tag{15}$$

With commercially provided dimensions of the cantilevers used in our system: $L = 240~\mu\text{m}$, $E = 160$ GPa, $G = 58$ GPa, $l = 10~\mu\text{m}$ and $t = 3~\mu\text{m}$, a value of the ratio is calculated as $S_{\text{ratio}} = 15.1$. The result indicates that the lateral voltage output, compared with the normal voltage output, is too weak to monitor the nanoparticle pushing operation. That is the reason why the normal voltage rather than the lateral voltage of the optical lever has been commonly used to monitor the pushing/pulling nanomanipulation [2]–[5], [9].

D. Controlled Push of Nanoparticles

In the literature, different types of nanoparticle push strategies, including contact and noncontact (dynamic) force microscopy, have been proposed. The former, with pushing control, is divided into the *constant height* and *constant force methods* [2]. The noncontact (dynamic) force microscopy utilizes the oscillating energy of the tip and tip-particle contact interactions to achieve a nanoparticle pushing operation. The main advantage of this method is the possibility of real-time monitoring of the moving particle. However, this method might be inefficient due to very the low power supply from the oscillating tip, compared with the energy dissipation needed to overcome the particle-substrate adhesion and friction [21], and investigations have shown that soft cantilevers (< 3 N/m) result in unsuccessful push [22].

In order to "see" the moving nanoparticle in real time and simultaneously achieve high-efficiency and stable pushing operations, as shown in Fig. 10, a dynamic pushing method is used in experiments, utilizing the advantages of the contact and noncontact pushing control methods. With this method, a constant distance d_0 between the tip and substrate is kept during the push. The tip-substrate separation d_0 is more or less equal to the radius R_p of the nanoparticle, which should provides enough maximum effective deflection D_0 to
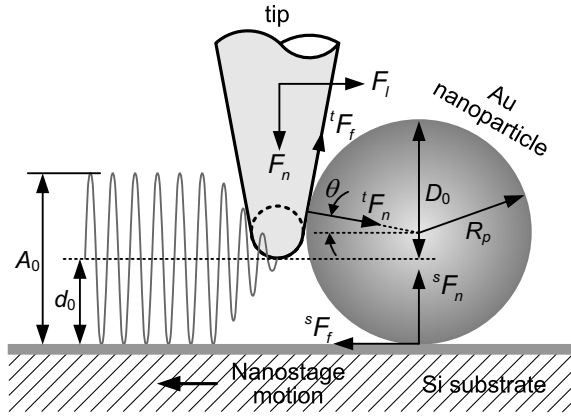
Fig. 10. Dynamic pushing schemes and interaction forces of the AFM tip apex and particle during pushing-sliding operation.

overcome strong static friction at the beginning of the push while the tip slides up the nanoparticle. Once contact with the nanoparticle is established, the amplitude of the oscillating tip reduces form A_0 to zero and the contact push is started. During pushing operations, the tip-nanoparticle contact may be lost, e.g. due to in-plane rotation/spinning of the nanoparticle as the result of a positioning error on the contact point or non-uniform interactions between the nanoparticle-substrate contact. In this case, the tip returns to oscillating with the same amplitude before contact; this, can be used to detect the contact loss automatically to restart the manipulation. This will be discussed in the following part.

During the pushing operation, possible nanoparticle motion modes are sliding, in-plane rotating and out-plane rotating (rolling). Fig. 10 shows an example of the interactive forces involved in the pushing-sliding motion of the nanoparticle. For other modes, detailed descriptions can be found in [9]. Let $^t F_f$ and $^t F_n$ be the friction force and the normal force applied on the nanoparticle due to the tip-nanoparticle interface, respectively. Therefore, to successfully push-slide the particle, a threshold force F_l^t along the push direction is needed:

$$F_l^t = {}^s F_f^{\max} = {}^t F_f \sin\theta + {}^t F_n \cos\theta, \qquad (16)$$

$$^t F_f^{\max} \geq F_l \sin\theta - F_n \cos\theta \qquad (17)$$

where $^s F_f$ and $^s F_n$ are the friction force and the repulsive force applied on the nanoparticle from the substrate, respectively; θ is the contact angle and its minimum value θ_{min} is equal to tip's half cone angle if tip-substrate separation d_0 is small enough; F_l and F_n are the lateral and the normal forces applied on the tip from the cantilever. For low speed and quasi-static pushing, it can be deduced that $F_l = {}^s F_f$ and $F_n = {}^s F_n$.

The friction force in nanoscale contact has been known to be proportional to the contact area A. Therefore, $^s F_f$ can be described by [23]:

$$^s F_f = \tau A \qquad (18)$$

where the proportional constant τ is the so-called shear strength. Consequently, the force needed to push the nanoparticle is proportional to the particle-substrate contact area A. The contact area depends on the interaction forces of the nanoparticle-substrate contact. According to the JKR model, the contact A of the nanoparticle with a radius R_p can be estimated from [24]:

$$A = \pi \left[\tfrac{R_p}{K}(F_{ext} + 3\pi R_p \Delta\gamma + \right.$$
$$\left. \sqrt{6\pi R_p \Delta\gamma F_{ext} + (3\pi R_p \Delta\gamma)^2}) \right]^{2/3} \qquad (19)$$

where $K = (4/3)[(1 - v_p^2)/E_p + (1 - v_s^2)/E_s]^{-1}$ is the reduced elastic modulus for the particle-substrate interface, in which v_p and v_s are the Poisson's coefficients, and E_p and E_s are the Young moduli of the nanoparticle and substrate, respectively; $\Delta\gamma$ is the particle-substrate critical energy needed to separate the nanoparticle from the substrate. Measuring $F_{ext} = {}^s F_n = F_n$ and using the known values of R_p, K, $\Delta\gamma$ and shear strength τ, the friction force $^s F_f$ can be calculated from (18).

When starting the push operation, the tip will slide up a little along the surface of the nanoparticle to obtain a new equilibrium. However, if the nanoparticle is too sticky to push or the cantilever is not stiff enough, the tip will slide up a lot, even slide over the nanoparticle, making the push unsuccessful. As the tip slides on the nanoparticle surface, the following inequality can be obtained:

$$^t F_f^{\max} < F_l \sin\theta - F_n \cos\theta. \qquad (20)$$

In order to successfully push the nanoparticle with the proposed dynamic pushing method, a cantilever with enough normal stiffness should be selected, and a proper contact angle θ be carefully determined. The contact angle θ can be set at its minimum value, i.e., the tip half cone angle, by reducing the tip-substrate separation d_0 to make a contact with the tip's cone surface providing that it does not result in a sticking problem. In our experiments, $k_n = 2.82$ N/m is used and the tip-substrate separation d_0 is set at less than the nanoparticle radius R_p to get a small contact angle θ and enough effective deflection D_0.

E. Manage Abnormity Status

1) Sticking Problem: The commercial AFM tip is very sharp (typically around 10 nm in radius), and that minimizes the adhesion forces between the nanoparticle and the tip. Nonetheless, unlike the nanoparticle push performed in liquid or vacuum [3], [25], the problem of nanoparticle sticking to the tip has been observed during nanoparticle push in ambient conditions, even in image scan with the AFM tapping mode. These phenomena are are mainly induced by the capillary forces [26]. In order to greatly reduce the possibilities of the particle sticking, it is necessary to modify the substrate to increase adhesion to the nanoparticle or functionalize the AFM tip, e.g., with hydrophobic interfaces that will strongly reduce adhesion to the nanoparticle. Moreover, environment control is also an effective method for changing the adhesion

forces. In our experiments, the environment is controlled with an ambient temperature of $20 \pm 1°C$ and relative humidity of $40 \pm 1\%$. In addition, nanoparticles with a diameter of about 80 nm are used and in contrast, the diameter of the AFM tip apex is much smaller. In this case, tip-particle adhesion forces are relatively lower than the particle-substrate interface. Therefore, the tip-particle sticking problem during the pushing operation can be minimized. The experimental results verified that sticking phenomena seldom occurred.

2) Particle Loss: A positioning error of the contact point and non-uniform interactions of the nanoparticle-substrate contact will result in in-plane rotation/spinning of the nanoparticle, especially over a long-distance pushing operation. Nanoparticle rotation/spinning leads to a push failure because of the contact loss. Second, strong static sticking of some nanoparticles to the substrate requires a stronger pushing force. Otherwise, the tip will slip over the nanoparticle, losing the push. In order to promptly detect the particle loss, as seen in Fig. 10, the tip II is kept in oscillation during the whole pushing procedure. By this means, not only can the tip-nanoparticle contact be detected by amplitude fading of the manipulating tip, but also the particle loss when the tip amplitude suddenly increases from zero.

V. EXPERIMENTAL RESULTS

High-speed image scanning is not yet available on the current system: that forms the basis of our future work on substantially improving nanomanipulation efficiency. However, a parallel image/manipulation task was first performed in air with normal-speed image scanning on the developed PIMM.

A. Sample Preparation

The manipulation samples were prepared by depositing 80 nm gold colloidal particles (Ted Pella, Inc) from an aqueous solution on freshly cleaned silicon substrates using the boiling method [27]. The Si substrate was placed on a hot plate that was set at an appropriate temperature of $100 \sim 110°C$. Drops of the gold nanoparticle solution were released on the substrate and were left to boil. The experiments were carried out in air (an ambient temperature of $20°C$ and relative humidity of 40%) with AFM probes with a spring constant of 2.82 N/m (ATEC-FM, Nanosensors).

B. Image Scanning Rate and Pushing Parameters

The imaging rate of the normal-speed scan and pushing parameters are set as follows:

- A scan frequency of 0.4 Hz on Tip II in tapping mode was used to fully scan the manipulation area of interest, e.g., for an image resolution of 200×200, the overall frame period of the image scan is about eight minutes and twenty seconds.
- The scan length on the end of tip II is set as about 40 nm, which results in a maximum scan height of 94 nm according to (1).
- Nanoparticle pushing velocity was set at about 200 nm/s and a small velocity of 80 nm/s was used for local nanoparticle scanning to achieve fine positioning.

- In the experiments, to improve the convergence rate of the particle repositioning and increase manipulation efficiency, a lower particle releasing accuracy is set at step length of the image scan, representing one pixel on the image plane.
- The tip-substrate separation d_0 during push was kept $10 \sim 20$ nm that depends on the nanoparticle diameter and snap-in boundary of the cantilever due to the adhesion forces.

C. Particle Loss Detection

Figure 11 how normal force and amplitude responses in a case of a successful gold nanoparticle (80 nm in diameter) push. When the tip snaps in the nanoparticle at point A, the oscillating amplitude disappears while starting the push. At point B, motion is started when static friction is broken, where the normal force on the cantilever is about $F_n = 24$ nN with a voltage output 18 mV (amplified) of the optical lever and force sensitivity 1.35 μN/V of the cantilever. From (18) and (19), the friction force is estimated as $^sF_f = 28$ nN. For calculation, $\Delta\gamma = 0.248$ J/m^2 is computed for SiO$_2$–Au contact in air with $\gamma_{SiO_2} = 0.16$ J/m^2, $\gamma_{Au} = 1.5$ J/m^2 and $\gamma_{H2O} = 0.073$ J/m^2; $K = 56$ GPa and $\tau \approx G^*/29 = 30$ MPa [28] with $G^* = [(2-\nu_{Au})/G_{Au} + (2-\nu_{SiO2})/G_{SiO2}]^{-1}$, where $G_{SiO_2} = 31.4$ GPa, $\nu_{SiO_2} = 0.17$, $G_{Au} = 30$ GPa, and $\nu_{Au} = 0.42$. With this friction force, the calculated (from (15)) and measured maximum lateral voltage output are both less than 3 mV, which is insufficient to monitor the pushing operation.

Figure 12 shows a cases of a nanoparticle loss at C point. Once the particle loss is detected, repositioning the nanoparticle is necessary to restart the unfinished push. As at the beginning of the push, a local scan on vertical and horizontal directions is used to relocate the lost nanoparticle with a scan distance of two to three times the nanoparticle's diameter. In the case of strong sticking friction from the substrate, tip-substrate separation d_0 is reduced to increase the maximum re-pushing force, or d_0 is even reduced to zero with normal preloading on the tip II for rare strong sticking cases.
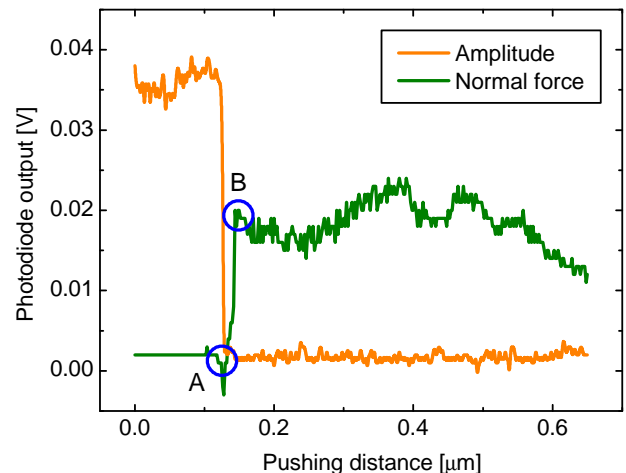

Fig. 11. A experimental example of tip II responses during a particle push: point A shows tip II snaps into contact with the nanoparticle, point B is where motion occurs when the static friction is broken.
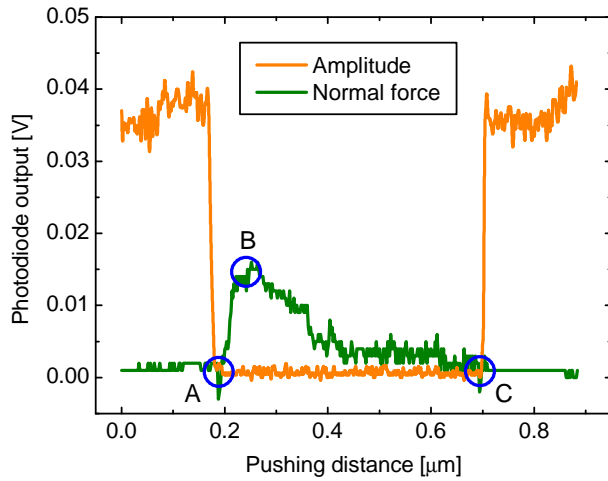
Fig. 12. A experimental example of tip II responses during a particle push then loss: point A shows tip II snaps into contact with the nanoparticle, point B is where motion occurs and point C is where the particle loss occurs.

D. Comparisons of Nanoparticle Parallel and Serial Push

With the settings described above, as seen in Fig. 13, the system was first tested by a lateral push of four gold nanoparticles; each particle was moved back and forth for four times between its original position and its target. The results show that no particle loss occurred; this might be due to a purely lateral push being used. In long-distance pushing, there is a greater tendency to rotation around the tip, resulting in larger pushing errors. The overall manipulation time, including nanoparticle positioning and pushing, is about $t_m = 320$ s, i.e, $t_m < t_s$, here $t_s = 500$ s. Thus, the task time of this work is $t_{\text{task}}^p = 2t_s = 1000$ s.

For comparison, a serial nanoparticle scan-manipulation-scan task was performed by Tip II. As seen in Fig. 14, four gold nanoparticles were also lateral pushed back and forth for four time as the same task in the above experiment. The overall manipulation time in this task is about $t_m = 280$ s. Thus, the task time $t_{\text{task}}^s = 2t_s + t_m = 1280$ s. By comparison, 28% more task time needed in this case than the former parallel nanomanipulation.

E. Parallel Manipulation Results

Figure 15 shows another parallel nanomanipulation result in which seven gold nanoparticles with a diameter of 80 nm, emerging in dynamic images I to IV in sequence, were pushed onto corners and the center of a regular hexagon during the period of the image scan. The frame period was about ten minutes. In contrast, the total manipulation time of these seven nanoparticles was less than seven minutes. The results indicate that more complex tasks can be completed during the image scanning thread, thereby greatly increasing the efficiency of AFM-based nanomanipulation.

In the experiments, image processing and task planning were first perform at the 95th (image I) and the 145th (image II) scan lines, which are, respectively, middle lines between the first and second, and second and third columns of the regular hexagon. After the 210th scan line, which is close to
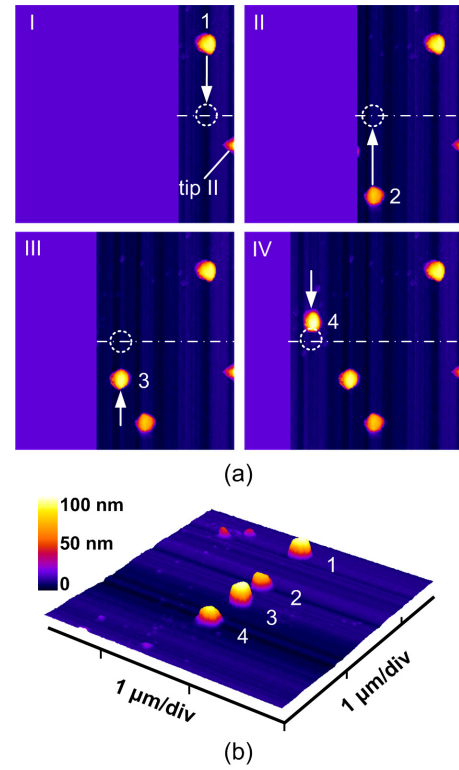

(a)

(b)

Fig. 13. Lateral push results with parallel manipulation (scan area 2.6 μm $\times$ 2.6 μm). (a) Dynamic image I to IV display emergences of four gold nanoparticles (with a diameter of $70 \sim 80$ nm). Image processing and task planning were performed every 16 scan lines that present the particle size on the image plane. (b) A post-manipulation image verifys the result. Each particle was pushed back and forth for four cycles between its original position and its target position before ultimately being placed on the target position on the middle line.
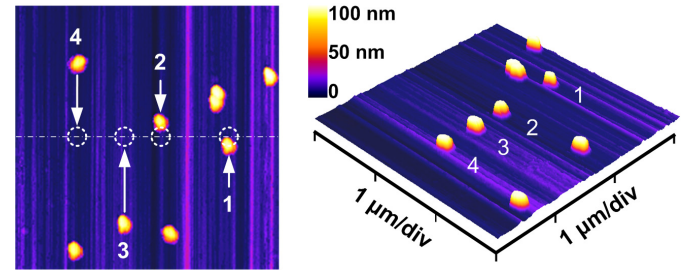

Fig. 14. Lateral push results with serial manipulation (scan area 3 μm $\times$ 3 μm). (a) Pre-scanned image of gold nanoparticles (with a diameter around 70 nm). (b) A post-manipulation image verifys that each particle was laterally pushed to its target position distributed on the middle line.

the left side of p_6 (image III), task planning had been arranged to perform once every 10 scan lines that present the particle size on the image plane. Fortunately, particles p_6 and p_7 were discovered in this frame. Thus, 3 times of image processing and task planning were performed during the whole process of manipulation.

From the experimental records, four particle losses occurred during the whole manipulation procedure, among which one for particle p_5, one for particle p_7 and two for particle p_6. It seems that the inward push along the long axis of the cantilever is more subject to pushing loss by sliding over the particle, which might to due to the large contact angle
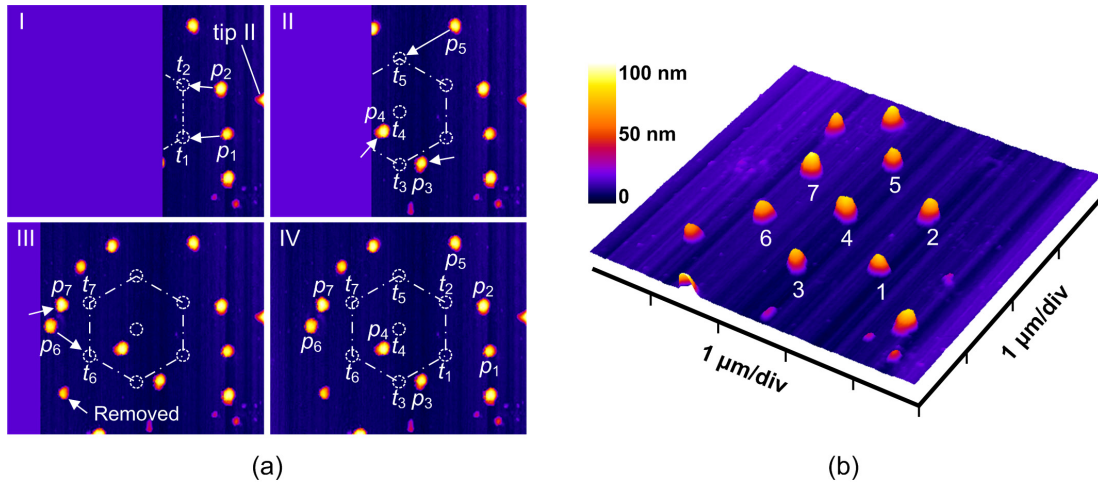
Fig. 15.   A parallel imaging/manipulation result with normal-speed image scan with tip I (scan area 4.8 μm × 4 μm). (a) Emergences of three parts of target positions and gold nanoparticles (with a diameter of 80 nm) are on three different dynamic displays, namely, image I to III. A full scan is shown in IV. (b) A post-manipulation image shows a regular nano-hexagon with a central nanoparticle is built with seven nanoparticles.

of about 52° from the side view of the titled tip. However, in this case, particle losses caused by in-plane rotation were seldom observed, which might be due to the contact with the backside of the cantilever's tetrahedral-shape tip. In contrast, the negative contact angle, which is about –22°, makes the forward push along the cantilever more vigorous. Additionally, apart from the final position check, a repositioning operation occurred five times to eliminate the final pushing error before releasing the particles on the target positions, once for particles p_1, p_2 and p_5 to p_7. A particle releasing accuracy is set at 20 nm, the step length of the image scan, representing one pixel on the image plane.

VI. CONCLUSION AND DISCUSSIONS

In this paper, a high-efficiency automated parallel imaging/manipulation microscopy was presented. Two automated parallel manipulation schemes with normal- and the high-speed image scanning were introduced. Experimental results validated the automated parallel manipulation scheme with normal-speed image scanning. Moreover, for the PIMM, many surprising achievements will be possible if high-speed image scanning is available and its potential applications are explored in future work. The problems or improvements to the PIMM's current use and potential applications are as follows:

1) High-speed image scanning with AFM tapping mode from several frames per second to video rate is not yet available in the current PIMM. In order to achieve such high-speed visual feedback of the parallel nanomanipulation, a special scanner with excellent dynamic performance, fast data acquisition facilities and smaller cantilevers with high resonant frequency should be used. The most significant step to meet these requirements would be to design and develop a high-speed image scanner able to promptly and accurately track the surface of nano-samples without image distortion, probe-induced nano-sample movement or damage.

2) The current system has been used for parallel manipulation of nanoparticles with a diameter around 80 nm.

It has been shown that the system positioning errors, e.g., system thermal drift, have no distinct influence on the manipulation. However, the influence from the positioning errors discussed cannot be omitted when the samples are scaled down to the order of 10 nm or less [29]. For the PIMM, with the two-tip configuration, characterization of the thermal drift between the tips and the nano-environment will be much more challenging than with conventional AFM.

3) For biology applications, nanomanipulation should crucially be performed in liquid. In this case, specific modifications to the current PIMM will be addressed, e.g., new scanner designs taking into account liquid flow instability, especially for high-speed image scanning.

4) Use of the PIMM we developed can be extended to other potential applications. For example, a new two-tip configuration, with a soft and a stiff cantilevers and minor modifications to the current system setup, can be used for well-controlled nanoparticle manipulation by the soft cantilever, allowing for the accurate extraction of quantitative values for nanoscale friction in ambient conditions, not just in vacuum [25]. This application will be of considerable interest because the stiff cantilever is generally needed in the commercial AFMs for nanoparticle imaging.

5) In addition, by reconfiguring the PIMM, a two-tip nanotweezer can be constructed for pick-and-place of nanowires/tubes with force sensing [30]. However, pick-and-place of nanoparticle is still a challenge using current system due to system's thermal drift that greatly influences the tip alignment accuracy. Thus, thermal drift characterization is a significant issue for future work.

As future work, high-speed image scan with the AFM tapping mode will be developed for achieving fast visual feedback on parallel nanomanipulation and greatly increasing the nanomanipulation efficiency based on the current configuration of the PIMM developed. In addition, manipulation in liquid will be addressed for biology applications.

This article has been accepted for publication in a future issue of this journal, but has not been fully edited. Content may change prior to final publication.

MANUSCRIPT TO IEEE TRANSACTIONS ON NANOTECHNOLOGY. PREVIOUS ID: TNANO-00155-2009   12

REFERENCES

[1] D. M. Eigler, and E. K. Schweizer, "Positioning single atoms with a scanning tunneling microscope," *Nature*, vol. 344, no. 6266, pp. 524–526, 1990.

[2] M. Sitti, and H. Hashimoto, "Controlled pushing of nanoparticles: modeling and experiments," *IEEE/ASME Trans. Mechatron.*, vol. 5, no. 2, pp. 199–211, June 2000.

[3] R. Resch, D. Lewis, S. Meltzer, N. Montoya, B. E. Koel, A. Madhukar, A. A. G. Requicha, P. Will, "Manipulation of gold nanoparticles in liquid environments using scanning force microscopy," *Ultramicroscopy*, vol. 82, no. 1–4, pp. 135–139, 2000.

[4] P. M. Albrecht, and J. W. Lyding, "Lateral manipulation of single-walled carbon nanotubes on H-passivated Si(100) surfaces with an ultra-high-vacuum scanning tunneling microscope," *Small*, vol. 3, no. 1, 146–152, 2007.

[5] E. Tranvouez, A. Orieux, E. Boer-Duchemin, C. H. Devillers, V. Huc, G. Comtet and G. Dujardin, "Manipulation of cadmium selenide nanorods with an atomic force microscope," *Nanotechnology*, vol. 20, no. 16, pp. 165304, 2009.

[6] X. Li, H. Gao, C. J. Murphy, and K. K. Caswell, "Nanoindentation of silver sanowires," *Nano Lett.*, vol. 3, no. 11, pp. 1495–1498, 2003

[7] B. Xu, and N. J. Tao, "Measurement of single-molecule resistance by repeated formation of molecular junctions," *Science*, vol. 301. no. 5637, pp. 1221–1223, 2003.

[8] L. Grill, K. Rieder, F. Moresco, S. Stojkovic, A. Gourdon, and C. Joachim, "Exploring the interatomic forces between tip and single molecules during STM manipulation," *Nano Lett.*, vol. 6, no. 12, pp. 2685–2689, 2006.

[9] M. Sitti, "Atomic force microscope probe based controlled pushing for nanotribological characterization," *IEEE/ASME Trans. Mechatron.*, vol. 9, no. 2, pp. 343–349, 2004.

[10] M. Palacio, and B. Bhushan, "A nanoscale friction investigation during the manipulation of nanoparticles in controlled environments," *Nanotechnology*, vol. 19, no. 31, pp. 315710, 2008.

[11] M. Bordag, A. Ribayrol, G. Conache, L. E. Fröberg, S. Gray, L. Samuelson, L. Montelius, and H. Pettersson, "Shear Stress measurements on InAs nanowires by AFM manipulation," *Small*, vol. 3, no. 8, pp. 1398–1401, 2007.

[12] L. X. Dong, F. Arai, and T. Fukuda, "Destructive constructions of nanostructures with carbon nanotubes through nanorobotic manipulation," *IEEE/ASME Trans. Mechatron.* vol. 9, no. 2, pp. 350–357, 2004.

[13] G. Y. Li, N. Xi, H. P. Chen, C. Pomeroy, and M. Prokos, "'Videolized' atomic force microscopy for interactive nanomanipulation and nanoassembly," *IEEE Trans. Nanotechnol.*, vol. 4, no. 5, pp. 605–615, 2005.

[14] W. Vogl, Bernice Kai-Lam Ma, and M. Sitti, "Augmented reality user interface for an atomic force microscope based nanorobotic system," *IEEE Trans. Nanotechnol.*, vol. 5, no. 4, pp. 397–406, 2006.

[15] G. T. Paloczi, B. L. Smith, P. K. Hansma, D. A. Walters, and M. A. Wendman, "Rapid imaging of calcite crystal growth using atomic force microscopy with small cantilevers," *Appl. Phys. Lett.*, vol. 73, no. 12, pp. 1658–1660, 1998.

[16] N. Kodera, H. Yamashita, and T. Ando, "Active damping of the scanner for high-speed atomic force microscopy," *Rev. Sci. Instrum.*, vol. 76, no. 5, pp. 053708, 2005.

[17] G. Schitter, K. J. Åström, B. E. DeMartini, P. J. Thurner, K. L. Turner, and P. K. Hansma, "Design and modeling of a high-speed AFM-Scanner," *IEEE Trans. Cont. Syst. Technol.*, vol, 15, no. 5, pp. 906–915, 2007.

[18] H. Xie, D. S. Haliyo, and S. Régnier, "Parallel imaging/manipulation force microscopy," *Appl. Phys. Lett.*, vol. 94, no. 15, pp. 153106, 2009.

[19] J. C. Russ, *The image processing handbook*, 5th Edition, CRC Press, Boca Raton, Florida, 2006.

[20] C. D. Onal, and M. Sitti, "Visual servoing-based autonomous 2-D manipulation of microparticles using a nanoprobe," *IEEE Trans. Cont. Syst. Tech.*, vol. 15, no. 5, pp. 842–852, 2007.

[21] M. Martin, L. Roschier, P. Hakonen, Ü. Parts, and M. Paalanen, B. Schleicher and E. I. Kauppinen, "Manipulation of Ag nanoparticles utilizing noncontact atomic force microscopy," *Appl. Phys. Lett.*, vol. 73, no. 11, pp. 1505–1507, 1998.

[22] R. Resch, A. Bugacov, C. Baur, B. E. Koel, A. Madhukar, A. A. G. Requicha, P. Will, "Manipulation of nanoparticles using dynamic force microscopy: simulation and experiments," *Appl. Phys A: Mater. Sci. Proces.*, vol. 67, no. 3, pp. 265–271, 1998.

[23] B. Bhushan, *Introduction to tribology*, New York: Wiley, 2002.

[24] K. L. Johnson, K. Kendall and A. D. Roberts, "Surface energy and the contact of elastic solids," *Proc. R. Soc. Lond. A*, vol. 324, no. 1558, pp. 301–313, 1971.

[25] D. Dietzel, T. Monninghoff, L. Jansen, H. Fuchs, C. Ritter, U. D. Schwarz, and A. Schirmeisen, "Interfacial friction obtained by lateral manipulation of nanoparticles using atomic force microscopy techniques," *J. Appl. Phys.*, vol. 102, no. 8, pp. 084306, 2007.

[26] K. Mougin, E. Gnecco, A. Rao, M. T. Cuberes, S. Jayaraman, E. W. McFarland, H. Haidara, and E. Meyer, "Manipulation of gold nanoparticles: influence of surface chemistry, temperature, and environment (vacuum versus ambient atmosphere)," *Langmuir*, vol. 24. no. 4, pp. 1577–1581, 2008.

[27] K. Lee, M. Duchamp, G. Kulik, A. Magrez, J. W. Seo, S. Jeney, A. J. Kulik, and L. Forro, "Uniformly dispersed deposition of colloidal nanoparticles and nanowires by boiling," *Appl. Phys. Lett.*, vol. 91, no. 17, pp. 173112, 2007.

[28] G. Dedkov, "Friction on the nanoscale: New physical mechanisms," *Materials Letters*, vol. 38, no. 5, pp. 360–366, 1999.

[29] B. Mokaberi, and A. A. G. Requicha, "Drift compensation for automatic nanomanipulation with scanning probe microscopes," *IEEE Trans. Autom. Sci. Eng.*, vol. 3, no. 3, pp. 199–207, 2006.

[30] H. Xie, D. S. Haliyo, and S. Régnier, "A versatile atomic force microscope for three-dimensional nanomanipulation and nanoassembly," *Nanotechnology*, vol, 20, no. 21, pp. 215301, 2009.

Hui Xie (S'05–M'07) received his B.S. degree in Mechanical Engineering from the Harbin University of Science and Technology, Harbin, China, in 2000, the M.S. degree in Mechanical Engineering and the Ph.D. degree in Mechatronics Engineering from the Harbin Institute of Technology, Harbin, China, in 2002 and 2006, respectively.

He became a Research Assistant in 2003 and Lecturer in 2005 at the State Key Laboratory of Robotics and System, Harbin Institute of Technology. He joined the Institut des Systèmes Intelligents et Robotique (ISIR), Université Pierre et Marie Curie/CNRS, France, as a postdoctoral Researcher in December 2006 and Research Associate in December 2008. His main research interests include microrobotics/nanorobotics, microscopic vision and automation on AFM-based nanomanipulation. His present research interests are parallel nanomanipulation force microscopy and 3D nanomanipulation force microscopy.

Dr. Xie received the Best Application Paper Award in the IEEE/RSJ International Conference on Intelligent Robots and Systems (IROS) 2009. He also received the Toshio Fukuda Best Paper Award in Mechatronics–Finalists in the IEEE International Conference on Mechatronics and Automation (ICMA) 2005.

Stéphane Régnier received his PhD degree in Mechanics and Robotics from the University of Pierre and Marie Curie, Paris, France in 1996.

He is currently Professor at the Institute of Intelligent Systems and Robotics (ISIR), University of Pierre and Marie Curie, Paris, France. He is head of the micromanipulation team of ISIR since 2001. His research interests are focused to micro and nano manipulation, teleoperation and haptic feedback at the nanoscale, micromechatronics and biological cell characterization.